

# Colon phantoms with cancer lesions for endoscopic characterization with optical coherence tomography

NATALIA ZULINA,<sup>1</sup> OSCAR CARAVACA,<sup>1</sup>  GUIQIU LIAO,<sup>1</sup> SARA GRAVELYN,<sup>1</sup> MORGANE SCHMITT,<sup>1</sup> KESHIA BADU,<sup>1</sup> LUCILE HEROIN,<sup>1,2</sup> AND MICHALINA J. GORA<sup>1</sup>

<sup>1</sup>*ICube Laboratory, CNRS, Strasbourg University, 1, Place de l'Hôpital - 67091 Strasbourg Cedex, France*

<sup>2</sup>*Gastroenterology Department, Hôpitaux Universitaires de Strasbourg, Strasbourg, France*

**Abstract:** Optical coherence tomography (OCT) is a growing imaging technique for real-time early diagnosis of digestive system diseases. As with other well-established medical imaging modalities, OCT requires validated imaging performance and standardized test methods for performance assessment. A major limitation in the development and testing of new imaging technologies is the lack of models for simultaneous clinical procedure emulation and characterization of healthy and diseased tissues. Currently, the former can be tested in large animal models and the latter can be tested in small animal disease models or excised human biopsy samples. In this study, a 23 cm by 23 cm optical phantom was developed to mimic the thickness and near-infrared optical properties of each anatomical layer of a human colon, as well as the surface topography of colorectal polyps and visual appearance compatible with white light endoscopy.

© 2021 Optical Society of America under the terms of the [OSA Open Access Publishing Agreement](#)

## 1. Introduction

According to the World Health Organization, colorectal cancer is the third most common cancer worldwide and is responsible for the second largest number of cancer deaths [1]. Endoscopic methods used to diagnose different types of colorectal diseases have difficulties in recognition of early neoplasia such as dysplasia and cancer *in situ*, and there is a need for development of novel advanced imaging methods. One such method is optical coherence tomography (OCT), a non-invasive optical imaging technology based on the principle of interferometry [2]. OCT provides cross-sectional images of internal tissue architecture with micrometer resolution, suitable for identification of tissue changes in the digestive system. In combination with white light endoscopy, it can be applied for real time diagnosis [3]. This can potentially decrease the cost and duration of patient care by excluding time-consuming processes like biopsy and pathological tests.

So far, in the digestive system, OCT has been most successfully applied for diagnosis of Barrett's esophagus [3]. Due to its high resolution, it is possible to differentiate OCT images of dysplastic mucosa from OCT images of nondysplastic mucosa. OCT characteristics of dysplasia are universal throughout the digestive system [4], which makes it highly prospective for colorectal pathologies diagnosis. OCT was tested as a possible tool for *in vivo* endoscopic differential diagnosis of colon polyps and assessing the need for their removal during colonoscopy [5–10].

Microscopic diagnosis of colorectal cancer with a complex geometry requires development of novel catheter designs for exploration of large areas of a colon, as well as verification during device development process before *in vivo* validation. To accelerate the development of such devices an appropriate testing model for verification of the system imaging performance and its feasibility for the clinical use is necessary. A variety of *in vivo* models have been used in pre-clinical cancer studies including the development of genetically modified rodents for the

use of OCT alone or in combination with fluorescence imaging [11–15]. Large animal models are superior in many aspects before a successful clinical translation as they have geometry and anatomy much closer to human in comparison to small animal models [16]. The limitation of large animal model use is the huge cost of disease development, caused in part by high housing and maintenance costs. In addition, a common problem for both small and large animal models is variation between animals, which makes it difficult to test reproducibility of a device.

To solve these problems, tissue and organ mimicking optical phantoms can potentially be applied and provide the opportunity to evaluate the performance of optical and spectroscopic instruments under controlled experimental conditions [4]. Such phantoms are an equivalent of an artificial tissue with well-controlled optical properties, which still must be specified according to the required anatomy of an organ of interest. A number of papers focused on quantitative studies of biological tissue optical properties provide mathematical and experimental framework for manufacturing and characterization/calibration of the optical properties of the phantoms [17–19]. A variety of materials and methods for producing optical phantoms with known or verifiable properties has already been published [4,20–26]. Tissue-mimicking phantoms have been produced using liquid media, and solid organic compounds such as gelatin, fibrin and agar [4,20]. These organic compounds have a limited shelf life (on the order of days) before they degrade and are not directly verifiable for the optical properties. The most common matrix materials in which the particles are suspended are: polyvinylchloride-plastisol [27], polyurethane and polyester resin [28] and silicone [4,22].

Silicone (PDMS) is a convenient base material for phantom fabrication. It provides ready compatibility with a wide range of suitable scatterers for adjustment of the optical properties. Even though PDMS does not have sufficient elasticity to mimic tissue stiffness phantoms, it allows for wrapping to mimic different shapes. PDMS is transparent in the VIS-NIR, and has a refractive index of 1.4, which is close to biotissue ranging from 1.35 to 1.55 [19].

Another prospective material with unique optical and highly viscous properties is a commercially available silicone-based liquid polymer, Dragon Skin (Smooth-On Inc.). Dragon Skin, which also has a refractive index of 1.4, has been used [4] to fabricate a 3D bladder phantom that simultaneously mimics healthy bladder tissue and its pathologies ranging from pre-cancerous dysplasia to muscle-invasive cancer.

The solid phantoms made of silicone-based materials have long term optical stability and greater shaping flexibility [29]. Their optical properties are controlled by the concentration of mixed absorber and scatterer. The solid phantoms usually have low absorption coefficients but relatively high scattering coefficients. The scattering objects are usually limited to aluminum oxide ( $\text{Al}_2\text{O}_3$ ), titanium dioxide ( $\text{TiO}_2$ ) and silicon dioxide ( $\text{SiO}_2$ ), polyester, polystyrene or latex microspheres.

There are also particle-free phantoms, with intrinsic scattering. Some phantoms fabricated this way use collagen, agarose, or even fibrin matrix [30] to encapsulate scattering intralipid solution or glycerol [31]. However, a drawback of such phantoms with intrinsic scattering lies in their short lifetime and reduced possibilities for introducing structures and creating multiple layers [32,33].

All anatomical layers of normal colonic tissue, such as mucosa and submucosa tissue, can be recognized in OCT images [34], while there is no evidence of any layered structures in the case of pathological tissue [35]. Thus, it is necessary to fabricate phantoms of organs with layered structures and mimic the optical properties of each tissue layer. Such phantoms have already been fabricated for other organs, including retina-mimicking phantoms developed to assess OCT image quality and software accuracy [36]. In our previous study, PDMS/ $\text{TiO}_2$ -based layered healthy colon tissue phantom was demonstrated [37]. Each layer was designed to emulate the optical properties, namely scattering, and the thickness of the corresponding anatomical layer. OCT tubular phantoms mimicking blood vessels [38] and irregular-shaped organ phantoms such

as the bladder with included different stages of cancer were previously published [4,39]. Other phantoms have been developed to perform image analysis [29], to characterize the resolution of systems [40], and to mimic tissue optical properties with biological contrast agents [30]. A fabrication technique has also recently been presented to mimic complex structures in flat tissues [20].

In this study, a PDMS/TiO<sub>2</sub> and Dragon Skin based phantom was developed and fabricated to mimic a 23 cm long section of human colon with layered healthy tissue and inserted benign and malignant colorectal lesions to accelerate development of novel optical imaging technologies. The multi-layered thin structure with an area of 529 cm<sup>2</sup> was achieved using a simple volume control method and superficial lesions were created using VeroWhite 3D-printed molds. The human colon optical phantom with colorectal cancer was developed with the following criteria: 1) realized full circumference geometry in three dimensions, 2) customizable material and optical properties, 3) mounting system allowing placement of lesions in various locations in the bench-top colon model (plastic or tissue) and removal using standard endoscopic tools, 4) visual appearance compatible with white light endoscopic imaging, and 5) long term stability.

The fabrication process involves layer-by-layer application of TiO<sub>2</sub> particle-embedded silicone films, with layer thickness controlled using material volume, followed by modification of the surface topography. To test the precision of the thickness control method using material volume the thickness distribution of layers was measured in a randomly selected regions mimicking healthy tissue using a bench-top OCT system and calculated using 3D-mapping algorithm. Endoscopic OCT imaging was performed inside the phantom using white-light flexible endoscopy. The phantom was used to quantify image quality of the OCT data obtained with a custom built endoscopic OCT system.

## 2. Methods

### 2.1. *Ex vivo swine bowel imaging*

A swept source OCT system built around a commercially available OCT engine (Axsun Technology) was used for imaging of excised swine bowel tissue and testing of optical properties of the developed phantom. The broadband laser source, centered at 1310 nm, provides tissue penetration of up to 1 mm with an axial resolution of 5.6 μm, and repetition rate of 100 kHz. For tissue imaging a bench-top mode with a galvo-scanner head and a lateral resolution of 25 μm was used. For modeling of attenuation of a bowel tissue, 50 OCT B-scan images of the various regions of healthy swine bowel tissue were used to measure the thickness of each layer.

### 2.2. *Phantom manufacturing*

To realize full geometry in three dimensions of the healthy tissue wall, the phantom is comprised of a silicone elastomer polydimethylsiloxane (PDMS) matrix and TiO<sub>2</sub> (Titanium (IV) oxide, 98%, anatase powder, Acros Organic). The PDMS (Sylgard 184, Dow Corning, USA) is a two component organic silicone, which cures at room temperature over 48 hours and remains flexible to allow for wrapping of the phantom. Heating effectively reduces curing time to minutes and allows for creation of complex, multilayer systems with internal structures. The biotissues usually have scattering coefficients that are two to three orders of magnitude higher than the absorption coefficients [20]. Since the phantom is developed for OCT working in the near-infrared range, we decided not to use nigrosine (usually used as an absorber), which has a much smaller impact on optical properties than TiO<sub>2</sub> introduced scattering in this wavelength range. To design the layered architecture of the healthy tissue (Fig. 1) we used previously published measurements showing an average thickness of human mucosa, submucosa and muscle layer to be 500 ± 100 μm, 250 ± 50 μm and 500 ± 100 μm, respectively [8,41].

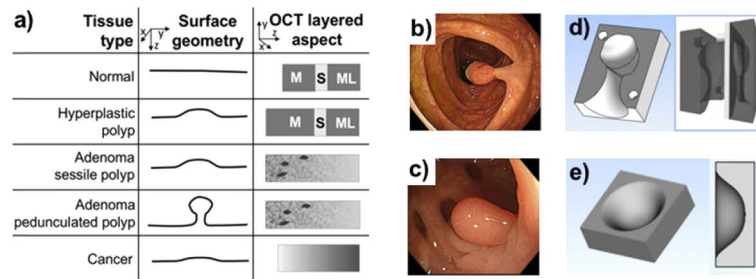


**Fig. 1.** (a) Schematic representation of design inputs for surface geometry and inner tissue architecture for most frequent tissue types [42]; Endoscopic image of (b) pedunculated polyp and (c) sessile polyp adapted with permission from [44]; CAD drawings of a mold for pedunculated polyp (d) and sessile polyp (e) phantom.

Polyp phantoms were made of highly viscous silicone-based two-part polymer DragonSkin. It is usually prepared by mixing parts in a 1:1 ratio by weight and is available in a variety of cure times ranging from 30 minutes to 16 hours. The fastest-curing Dragon Skin, FX-Pro, has been used for fabrication of the phantom in this study. Colorectal lesions most typically present in the colon are polyps of two types: pedunculated and sessile [42]. The required shapes of phantom polyps (Fig. 1) were established based on the official classification of lesions in the digestive system, that is used by gastroenterologists to diagnose diseases [43].

To mimic the aspect of dysplastic tissue glycerol material was used. Glycerol is a viscous transparent in the VIS-NIR wavelength range liquid. It is used primarily as an optical clearing agent [45], but it has also been used as a matrix material for liquid, particle-based phantoms [46]. This mixture creates an emulsion which is stable after curing and forms bubbles that mimic dysplastic glands of the adenoma polyps. The sessile polyps, which are low, dome like structures, were developed using a single mold (Fig. 1(e)). It was first filled out with the Dragon Skin and glycerol mixture and then a small neodymium magnet was submerged just below the surface before curing. The pedunculated polyps, which have a tree-like structure were developed using a two part mold to enable removal of the polyp (Fig. 1(d)).

In this work we combine various manufacturing methods and materials in order to develop a fast method of phantom fabrication. The phantom is designed as stable and flexible with the possible introduction of structural inhomogeneities. The fabrication process is shown in Fig. 2. and is described in detail in the step by step procedure below:

Steps 1–3: In the first three steps a normal colon wall was manufactured, comprising muscle layer, submucosa and mucosa. For each layer a required amount of  $\text{TiO}_2$  (1.2 mg/mL for mucosa, 10 mg/mL for submucosa and 2.2 mg/mL for muscle layer) was added to the curing agent in the graduated tube and stirred for 30 seconds, using the spatula. It was then mixed together with the second components of PDMS according to the manufacturers' advised quantities of 10:1 parts by volume, a ratio of the base PDMS material to the curing agent volumes. Air was evacuated from the mixture in a vacuum chamber. The mixture was poured into a rectangular (23×23 cm) aluminum mold. The required layer thickness was controlled by a volume amount calculated using the size of the mold. Each layer was heated to 80°C for 60 minutes to solidify it before adding the next layer. During PDMS solidification in the mold, the phantom slightly wraps at the edges.

Steps 4-5: To imitate neoplastic, flat (invasive) lesions, a small circular piece of layered structure was cut using a scalpel and removed. The lesion gap was filled with a high concentration mixture (over 1% wt) of  $\text{TiO}_2$  in PDMS.

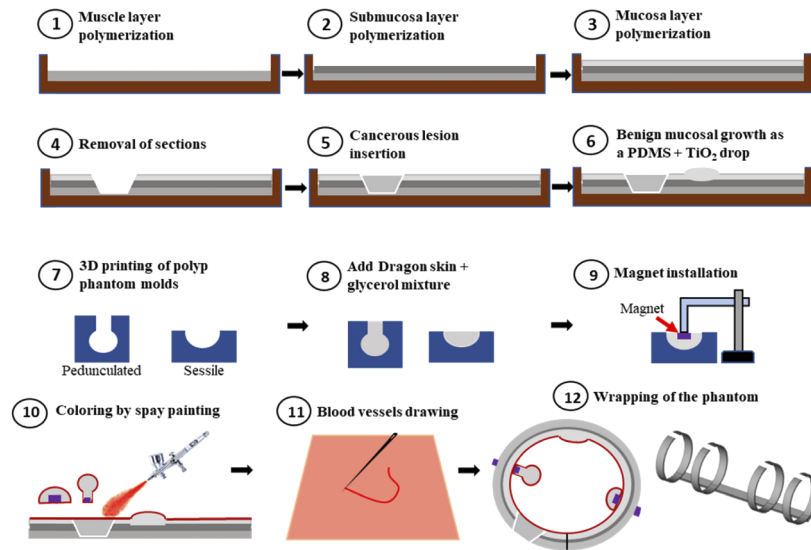


**Fig. 2.** Process diagram for the fabrication of a colon phantom with flat cancerous lesion, pedunculated and sessile polyps.

Step 6: For a superficial hyperplastic polyp phantom a drop of PDMS/TiO<sub>2</sub> mixture mimicking the mucosa layer was used, to mimic a nonneoplastic mucosal growth. The drop was polymerized at room temperature.

Step 7: To manufacture the pedunculated and sessile polyps, first phantom molds were designed in 3D CAD software (PTC Creo) and 3D printed in VeroWhite resin (Connex 350, Stratasys) with a Stratasys PolyJet printer. The pedunculated polyp mold was a two part mold to enable its opening for removal of the polyp.

Step 8: For dysplastic lesions, such as adenoma, two parts of Dragon Skin FX-pro (Smooth-On Inc.) polymer were prepared by mixing parts A and B in a 1:1 ratio by weight. Then Dragon Skin compounds were mixed in 1:10 ratio with glycerol to mimic dysplastic glands (98% Prolabo, Paris) and with polydisperse charcoal particles to mimic scattering of a low grade lesions.

Step 9: Before curing, to enable attachment and testing of polyp removal, 3 mm neodymium magnets were inserted in the polyp and used to attach obtained phantoms to the PDMS layered colonic wall.

Step 10: The healthy tissue base and polyps were colored using an airbrush tool and silicone-based polymer (Psycho Paint resin pro, Smooth-On Inc.). A mixture of yellow, beige and red pigments were used to simulate human tissue coloring, and Novocs solvent (200-500% wt, Smooth-On Inc.) was used to lower viscosity and make the spraying process with a mini airbrush compressor T-100 (KKmoon) easier. The Phantom was dried for 24 hours.

Step 11: Blood vessels were drawn on the phantom surface with a needle, on which a small amount of Psycho Paint resin with a red-yellow mixture of pigments was applied.

Step 12: The phantom was wrapped to mimic colon circumference geometry, then inserted in a plastic cage structure, which stabilized the lumen and added the aspect of colonic folds.

### 2.3. Optical properties and 3D thickness mapping

To confirm that the optical properties of the developed phantom have the correct attenuation profile we measured an excised swine bowel in a custom built bench-top OCT system with an Axsun 1310 nm engine. Averaged profiles of 50 A-lines were extracted using ImageJ software for comparison between the attenuation profile of *ex vivo* swine bowel and the developed healthy



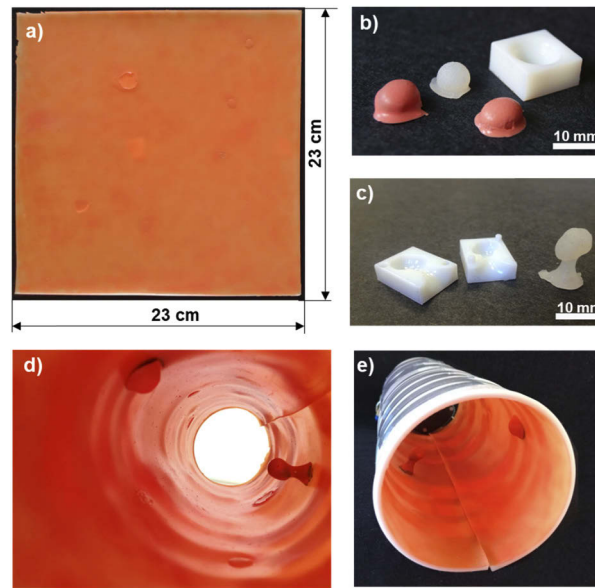


**Fig. 3.** (a) Unfolded 23 cm by 23 cm colon phantom with cancerous insertions and benign polyps (before blood vessels drawing). 3D-printed VeroWhite molds for (b) sessile and (c) pedunculated polyp phantoms. (d) internal and (e) external views of the folded colon phantom.

tissue phantom (Fig. 4). Average OCT intensity was calculated for each layer of both swine bowel and phantom, then OCT intensity ratios between the submucosa/mucosa (S/M) and submucosa/muscle layer (S/ML) were obtained.

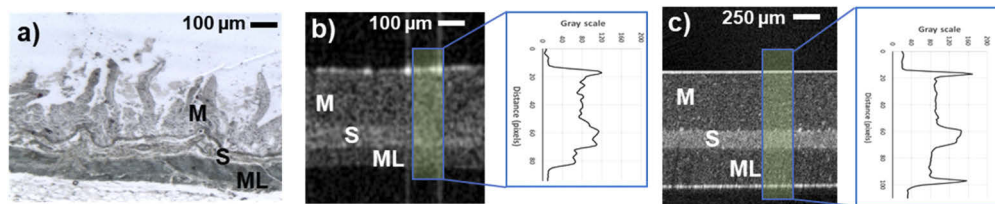


**Fig. 4.** (a) Histology of a swine bowel tissue. OCT images and intensity plots of 50 averaged A-scans of (b) swine bowel *ex vivo* and (c) phantom. Scale bar represents a physical size.

Two-dimensional B-scans and three-dimensional data of the various regions of the phantom were acquired on the unwrapped phantom (Fig. 5). The 3D reconstructions of all lesion types were obtained using ImageJ software. All OCT data presented in this paper represent physical distances where refractive indices of 1.4 and 1.38 were taken into account for the phantom and a swine bowel, respectively. Correction of refraction was especially crucial for cross-sectional images of polyps where dome like structures caused artificial deepening of underlying layers [47].

To verify the precision of a thickness control using material volume, a 3D dataset (contains 300 frames) was acquired using the bench-top OCT system. A three-dimensional layer mapping for a 6 mm × 6 mm area (measured by top-view) was modeled for analysis of thickness distribution. We developed an automatic layer segmentation algorithm to process the individual image, which utilizes a path searching algorithm based on a line-segmentation [48,49] to segment the continuous

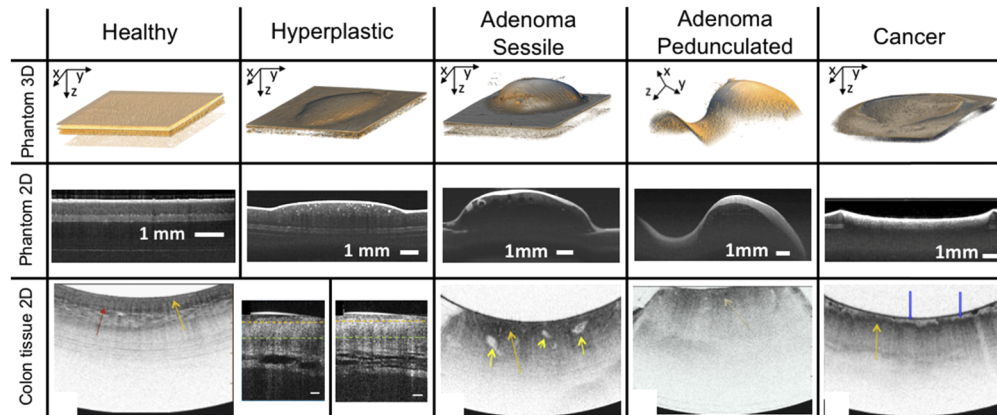


**Fig. 5.** Volumetric rendering of 3D OCT data and cross-sectional OCT images of different tissue types present in the phantom obtained with a custom benchtop imaging system and compared with OCT images of corresponding tissue types obtained in human adapted with permission from [50,54]. The volumetric data for the pedunculated polyp was acquired from its side to better present its shape.

layer boundaries within each OCT frame. Following cropping of the area of interest we applied a peak searching process [49] to find 4 peaks position at the leftmost A-line of the image, which represent the starting points of a lumen contour and layer boundaries. After that the cropped image is convoluted with an edge detection kernel to get an edge map [48]. Finally, by searching four continuous paths on this edge map with determined starting points, the lumen contour and layer boundaries are segmented. After applying the segmentation algorithm to this image sequence, all segmented results were concatenated to show the relative boundary positions of the three-dimensional reconstruction. All the algorithm codes were implemented with Python. The OpenCV package was used to do filtering and pre-processing over the original OCT images. The thickness map results are generated with Matlab software, and the 3D model is rendered with ImageJ software.

#### 2.4. Endoscopic OCT test of the colorectal cancer phantom

To test if the proposed method can be used to test safety and feasibility of novel devices and their compatibility with a current standard of care we performed an endoscopic examination of the phantom. The key question was if the phantom can be used for an endoscopic examination similar to the standard of care procedure and to test the performance of an accessory imaging device. As during the standard of care examination the endoscopist was asked to detect abnormal lesions and render their diagnosis.

The OCT imaging system was connected to a custom built endoscopic OCT catheter. The low profile OCT catheter with a custom built proximal scanning actuator build around a commercially available rotary joint (Princetel) and a three layer driveshaft with an outer diameter of 0.9 mm (Asahi Inc.) was used to obtain 2D OCT images. The near infrared light was side-focused just outside of the plastic sheath with an outer diameter of 1.6 mm to a spot of 30  $\mu\text{m}$  using a 0.26 mm ball lens (IDIL).

The OCT probe was inserted using a working channel of standard gastroscope (Karl Storz, 13821PKS, Sliver line) with illumination xenon light source, a video processor and a monitor (Fig. 6). A gastroenterologist inserted the scope and explored various areas of the phantom using endoscopic video side-by-side to OCT real-time images. Simultaneous recording of white-light endoscopy and OCT videos was performed. The procedure included white-light

endoscopy surface visual inspection and OCT probe contact sliding along the suspicious areas performed by a gastroenterologist not familiar with the phantom fabrication process. Once an abnormal lesion was detected visually in the endoscopic image, it was examined in greater detail with the OCT probe. Based on an assessment of the shape (flat, depressed, or elevated) and color (pale or reddened), superficial lesions phantoms were identified and characterized by experienced endoscopists. Each polyp phantom was sequentially studied with the OCT probe for differentiating hyperplastic, adenomatous and carcinomatous polyp phantom types by comparing with Refs. [9–11].

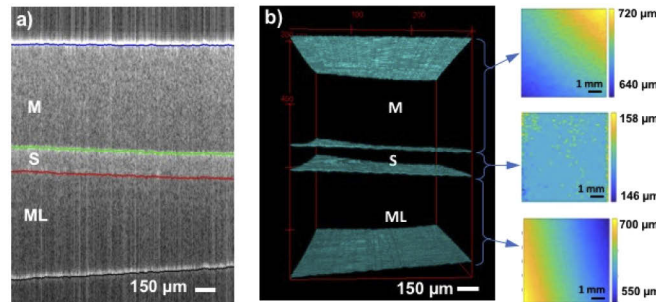


**Fig. 6.** Thickness analysis of a 6 mm by 6 mm area of the phantom mimicking normal tissue. (a) Segmentation of 2D OCT image with mucosa (M) in between blue and green lines, submucosa (S) between green and red lines and muscularis layer (ML) between red and black line. (b) Reconstructed 3D view of automatically segmented layers and corresponding 2D thickness maps of mucosa (top), submucosa (middle) and muscularis layer (bottom).

To quantitatively analyze the performance of the endoscopic OCT, its noise, SNR and contrast were compared to a bench-top images and OCT images from the colon obtained with a commercialized endoscopic OCT for surveillance of the esophagus called Volumetric Laser Endomicroscopy (VLE) [50]. For noise performance analysis, two 400×400 pixels windows to select blank area without a tissue, and the region of interest (ROI) area which contains all the 3 layers are used. We normalized all the images by the maximum value of ROI images. We used background intensity mean-variance value  $I_{vb}$  as the amplitude of the overall noise, to calculate the SNR value  $r$  by formula  $r = 20 \log(I_m/I_{vb})$ , where  $I_m$  is the max intensity of the ROI. To calculate local contrast at different positions small rectangular windows of 100×50 pixels are placed at lumen contour or layer boundaries [51]. Five rectangular windows are taken for each lumen contour or layer boundary in each frame. The contour and boundaries divide the operation windows into two parts, and 3×3 median filters are applied to these two parts separately to remove speckle noise. Then the local contrast value  $S$  is calculated by  $S = |E_1 - E_2| / (E_1 + E_2)$  [52], where  $E_1$  and  $E_2$  are the mean intensity values of pixels above and below the lumen contour or layer boundaries.

### 3. Results

#### 3.1. Developed colon phantom

Figure 3 shows the developed colon phantom with inserted colorectal lesions. Using a large mold, normal colon tissue with embedded flat cancerous insertions and benign flat polyps with a size of 23 cm by 23 cm was achieved. The sessile and pedunculated polyps, developed using 3D printed custom molds (Figs. 3(b) and 3(c)), can be inserted in any location of the phantom using neodymium magnets placed on the outside of the phantom.



Using an external plastic cage structure, the flexible tissue phantom was folded to create a colon section (Figs. 3(d) and 3(e)). Shape and size of the phantom corresponds well with the inflated descending part of the human colon during white-light endoscopy [53].

### 3.2. Optical properties and thickness distribution of a normal tissue phantom

The fabrication process of normal tissue involved layer-by-layer formation of PDMS films doped with  $\text{TiO}_2$  [36]. The concentration of scatterers was adjusted to obtain corresponding contrast in the tissue-mimicking phantom with concentrations of 0.2, 1 and 0.1%wt, for mucosa, submucosa and muscularis layers, respectively. The cross-sectional OCT images of the normal tissue phantom and excised swine bowel show good agreement with histology (Fig. 4). Comparison of the intensity profiles of the phantom and the swine bowel shows the difference of 7% and 10% in contrast between mucosa and submucosa layers, and submucosa and muscle layers, respectively.

The cross-section of a phantom wall with normal tissue characteristics (Fig. 5) can be also compared to previously published OCT images from the human colon obtained with a balloon based volumetric laser endomicroscopy catheter commercialized for intended use in the esophagus (left) [50] and a forward viewing probe (right) [54]. Qualitatively, the layered architecture of the phantom is comparable to the real tissue structure. The results published using a forward viewing probe provide a unique comparison of a normal tissue to a hyperplastic polyp. As can be seen, the hyperplastic tissue is very similar to the healthy tissue with the main difference in thickness of the mucosa. The thickening of the mucosa in the phantom's hyperplastic polyp can be clearly observed on the cross sectional OCT image and 3D reconstruction (Fig. 5). The lack of layered architecture with higher surface reflectivity and presence of glandular structures are typical features used for identification of abnormal lesions. An exemplary OCT cross-section of a sessile adenoma phantom polyp shows multiple glandular structures created by the addition of the glycerol. Such structures can be also observed in OCT image obtained with a VLE catheter from a polyp with high-grade dysplasia. The developed pedunculated polyp, on the other hand, has a lack of layering but no visible glands, which is similar to a VLE example of a tubulovillous adenoma. A VLE image of a cancerous tissue shows lack of layered structure and visually higher scattering at the surface that decreases intensively with depth. Similar image features can also be observed in the OCT cross-section of the flat cancerous lesion inserted in the phantom wall.

To test thickness accuracy of the proposed thickness control method based on material volume a randomly selected  $6\text{ mm} \times 6\text{ mm}$  area of the normal tissue was imaged with the bench-top OCT system. Using the developed automatic segmentation software, the boundaries of all layers were identified (Figs. 6(a) and 6(b)). The layer thicknesses were quantified and represented in thickness maps (Figs. 6(c)–6(e)) to show layer thickness distribution. Varying thickness can be observed across the imaging area of the first and the third layer. The thickness of the first layer is uniformly increasing from  $640\text{ }\mu\text{m}$  to  $720\text{ }\mu\text{m}$ , and the thickness of the third layer is decreasing from  $700\text{ }\mu\text{m}$  to  $550\text{ }\mu\text{m}$ , which can be attributed to small tilt of the mold during PDMS curing process. The middle layer, representing submucosa, has a thickness of  $150 \pm 10\text{ }\mu\text{m}$ . Mold tilt did not effect this layer thickness distribution significantly due to surface tension and the high viscosity of PDMS.

### 3.3. Endoscopic OCT test of the colon phantom

The first part of this study was focused on accurate emulation of mechanical properties of the phantom. To achieve a good maneuverability of the endoscope the colon phantom was attached to a plastic box with endoscope insertion entry as shown on Fig. 7(a). The endoscopic probe with an OCT catheter in a working channel (Fig. 7(b)) was inserted in a colon phantom (Fig. 7(c)). Retroflexion inside the phantom obtained with a  $150^\circ$  turn of the endoscope end is shown in Fig. 7(d) for demonstration of size correspondence of the phantom to a real organ. To mimic the

presence of mucus, coconut oil was applied to the phantom surface to lower the friction of the endoscope and allow smooth sliding along the phantom wall for continuous scanning.

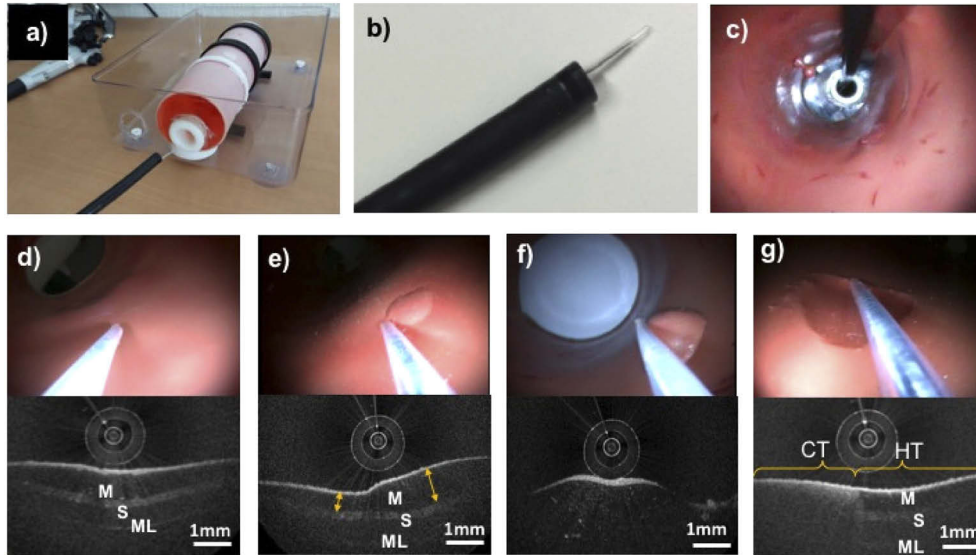


**Fig. 7.** White light endoscopy and OCT examination of the colon model. (a) External view of the assembled colon phantom. (b) Picture of the OCT catheter inserted in the working channel of the endoscope. (c) Internal view of phantom with visible lesions and folds during retroflexion examination inside the phantom obtained with a 150° turn of the tip of the endoscope. Endoscopic images and corresponding OCT cross-sections of (d) healthy tissue with layered architecture of mucosa (M), submucosa (S) and muscular layer (ML), (e) non neoplastic mucosal growth phantom, representing a benign lesion with visible thickening of the mucosa (yellow arrows), (f) pedunculated polyp phantom, and (g) flat cancerous tissue (CT) on the left, next to the healthy tissue (HT) sessile.

Using white light video, the OCT catheter was placed close to various areas of the phantom surface to obtain the images. The pink colonic wall of the 23 cm long segment with added dark red vessel like structures can be observed in Fig. 7(c). Healthy colon tissue phantom is presented in Fig. 7(d). Similar to benchtop OCT images, it is a layered structure, consisting of mucosa, submucosa and muscle layer, with different scattering coefficients [55]. In another location of the phantom a hyperplastic polyp can be seen as an elevated area in the white light endoscopy image (Fig. 7(e)). A corresponding OCT cross-section shows thickening of the mucosa with no disruption to the continuity of the underlying submucosa layer. An exemplary endoscopic image of the pedunculated sessile polyp (Fig. 7(f)) shows irregular scattering distribution throughout the volume of the polyp with no internal layers. The 3D printed pedunculated and sessile polyps can be attached in any locations of the lumen by placing a neodymium magnet on the outside of the phantom. The flat, malignant, and most suspicious dysplastic lesion is shown on Fig. 7(g). The surface layer of such tissue has higher scattering that decreases in bulk with no evidence of layered structure. Such visual characteristics of high tissue reflectivity has been previously reported in experimental studies of optical properties of malignant tissues and OCT imaging since it has less collagen than is present in normal tissue [9,50].

We also used the phantom to provide quantitative analysis of the imaging performance of the custom endoscopic OCT device, which we compare to bench-top images of the phantom and human colon images obtained with a commercially available VLE catheter (Fig. 8). As can be seen in Fig. 8 the custom catheter has the highest background intensity, and the highest

background noise. The benchtop mode has the lowest background intensity and derivation. The higher noise in both custom and commercialized catheters can be attributed to larger number of artifacts caused by backreflection from the micro-optics and the sheath. The custom catheter has the lowest SNR value of 26.85 dB, whilst the benchtop images has the highest SNR value of 39.93 dB. As can be expected, the contrast between the mucosa and submucosa layers, and submucosa and muscle layers is lower than the contrast between the air and the top mucosa layer, no matter what device is used for scanning. Nevertheless, the bench top images show better contrast than the other two devices, especially for the third boundary, which can hardly be seen in catheter images (with a contrast rate of 0.32). Detailed statistical information is given in Table 1.

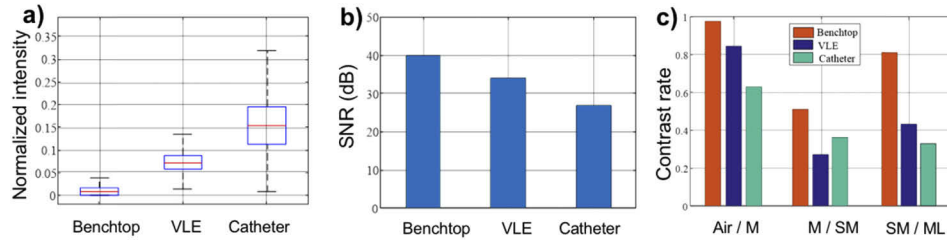


**Fig. 8.** Image quality analysis showing: (a) background intensity distribution, (b) SNR and (c) local contrast of the OCT phantom images obtained with the custom catheter and a bench-top mode, compared to OCT images of the human colon from a commercial volumetric laser endomicroscopy (VLE).

**Table 1. Image quality comparison**

	Custom catheter & phantom	VLE & human colon [50]	Custo bench top & phantom
SNR	26.85dB	33.97dB	39.93dB
Lumen contour contrast rate	$0.628 \pm 0.048$	$0.845 \pm 0.008$	$0.976 \pm 0.004$
L1(top layer) vs L2 contrast rate	$0.361 \pm 0.203$	$0.269 \pm 0.103$	$0.507 \pm 0.330$
L2 vs L3 contrast rate	$0.328 \pm 0.261$	$0.429 \pm 0.123$	$0.810 \pm 0.374$

#### 4. Conclusions

In this work an OCT phantom of a human colon with realistic optical properties was obtained, as well as the morphology of healthy tissue and lesions typical for colorectal cancer. This phantom may serve as a convenient tool to evaluate and standardize OCT image quality and measurement accuracy. Such a performant standardization can lead to improved performance of measurements from clinical and research OCT devices, thus enhancing reliability of diagnostic decisions and facilitating the development of innovative diagnostic technologies.

We propose here a simple method for thickness control based on volume control. This method is less precise than previously proposed methods but enables development of a larger phantom. In addition, as it was shown in previous studies that mucosal/submucosal thickness may vary through specimen length and also from healthy to pathological stages [6]. There is a thickness distribution with tolerance bar range of 50-100  $\mu\text{m}$ .

We used 3D printing for phantom polyp molds to mimic real shapes and sizes. To enable placement of polyps in various locations and their removal, training magnet mounts were used to attach the phantom polyps to the flat bowel-mimicking phantom.

One limitation of this study is the use of animal tissue to model the layered distribution of the healthy tissue. However, swine's digestive system is the closes model to the human and is

commonly used in imaging procedures, as well as for testing of novel surgical treatment options. It is important to mention that the proposed method of the development of the large geometry optical phantom is very versatile and both thickness and scattering properties can be easily adjusted making it a suitable method for the development of phantoms of different organs. We also present only one type of sessile and one type of pedunculated polyp, but different polyp morphology, as well as morphology typical for other diseases, can be easily obtained using CAD software and rapid prototyping that typically has precision of few hundred microns.

The continued advancement of novel optical imaging technologies for improved diagnosis of colorectal cancer depends upon the development of reproducible and reliable phantoms. New large organ phantoms fabrication strategies that can better mimic the structure, surface topology and optical properties are necessary. This research will assist in efforts to design such phantoms, which could then form the basis for verification tests and durable, transferable standard imaging targets for OCT and other optical imaging technologies.

## Funding

ATIP-Avenir 2016, Fondation ARC pour la Recherche sur le Cancer; University of Strasbourg's IdEx program; European Union's Horizon 2020 research and innovation programs under the H2020 Marie Skłodowska-Curie Actions (813782).

## Acknowledgements

The authors would like to thank Dr. Lam Chanh Dao for performing the histology, Dr. Cristina Antal for pathology reading and Dr. Xingde Li for MATLAB codes sharing.

## Disclosures

The authors declare no conflicts of interest.

## References

1. "Cancer," <https://www.who.int/news-room/fact-sheets/detail/cancer>.
2. T.-H. Tsai, J. G. Fujimoto, and H. Mashimo, "Endoscopic Optical Coherence Tomography for Clinical Gastroenterology," *Diagnostics* **4**(2), 57–93 (2014).
3. M. J. Gora, J. S. Sauk, R. W. Carruth, K. A. Gallagher, M. J. Suter, N. S. Nishioka, L. E. Kava, M. Rosenberg, B. E. Bouma, and G. J. Tearney, "Tethered capsule endomicroscopy enables less invasive imaging of gastrointestinal tract microstructure," *Nat. Med.* **19**(2), 238–240 (2013).
4. G. T. Smith, K. L. Lurie, D. V. Zlatev, J. C. Liao, and A. K. Ellerbee Bowden, "Multimodal 3D cancer-mimicking optical phantom," *Biomed. Opt. Express* **7**(2), 648–662 (2016).
5. S. Jäckle, N. Gladkova, F. Feldchtein, A. Terentjeva, B. Brand, G. Gelikonov, V. Gelikonov, A. Sergeev, A. Fritscher-Ravens, J. Freund, U. Seitz, S. Soehendra, and N. Schröder, "In vivo endoscopic optical coherence tomography of the human gastrointestinal tract—toward optical biopsy," *Endoscopy* **32**(10), 743–749 (2000).
6. P. R. Pfau, M. V. Sivak, A. Chak, M. Kinnard, R. C. K. Wong, G. A. Isenberg, J. A. Izatt, A. Rollins, and V. Westphal, "Criteria for the diagnosis of dysplasia by endoscopic optical coherence tomography," *Gastrointest. Endosc.* **58**(2), 196–202 (2003).
7. P.-L. Hsiung, L. Pantanowitz, A. D. Aguirre, Y. Chen, D. Phatak, T. H. Ko, S. Bourquin, S. J. Schnitt, S. Raza, J. L. Connolly, H. Mashimo, and J. G. Fujimoto, "Ultrahigh-resolution and 3-dimensional optical coherence tomography ex vivo imaging of the large and small intestines," *Gastrointest. Endosc.* **62**(4), 561–574 (2005).
8. V. Westphal, A. M. Rollins, J. Willis, M. V. Sivak, and J. A. Izatt, "Correlation of endoscopic optical coherence tomography with histology in the lower-GI tract," *Gastrointest. Endosc.* **61**(4), 537–546 (2005).
9. E. Zagaynova, N. Gladkova, N. Shakhova, G. Gelikonov, and V. Gelikonov, "Endoscopic OCT with forward-looking probe: clinical studies in urology and gastroenterology," *J. Biophotonics* **1**(2), 114–128 (2008).
10. D. C. Adler, C. Zhou, T.-H. Tsai, J. Schmitt, Q. Huang, H. Mashimo, and J. G. Fujimoto, "Three-dimensional endomicroscopy of the human colon using optical coherence tomography," *Opt. Express* **17**(2), 784–796 (2009).
11. A. R. Tumlinson, B. Považay, L. P. Hariri, J. McNally, A. Unterhuber, B. Hermann, H. Sattmann, W. Drexler, and J. K. Barton, "In vivo ultrahigh-resolution optical coherence tomography of mouse colon with an achromatized endoscope," *J. Biomed. Opt.* **11**(6), 064003 (2006).

12. S. Yuan, C. A. Roney, J. Wierwille, C.-W. Chen, B. Xu, G. Griffiths, J. Jiang, H. Ma, A. Cable, R. M. Summers, and Y. Chen, "Co-registered optical coherence tomography and fluorescence molecular imaging for simultaneous morphological and molecular imaging," *Phys. Med. Biol.* **55**(1), 191–206 (2010).
13. N. Ifimia, A. K. Iyer, D. X. Hammer, N. Lue, M. Mujat, M. Pitman, R. D. Ferguson, and M. Amiji, "Fluorescence-guided optical coherence tomography imaging for colon cancer screening: a preliminary mouse study," *Biomed. Opt. Express* **3**(1), 178–191 (2012).
14. R. A. Wall, G. T. Bonnema, and J. K. Barton, "Novel focused OCT-LIF endoscope," *Biomed. Opt. Express* **2**(3), 421–430 (2011).
15. R. A. Wall and J. K. Barton, "Fluorescence-based surface magnifying chromoendoscopy and optical coherence tomography endoscope," *J. Biomed. Opt.* **17**(8), 086003 (2012).
16. K. M. Schachtschneider, R. M. Schwind, J. Newson, N. Kinachtchouk, M. Rizko, N. Mendoza-Elias, P. Grippo, D. R. Principe, A. Park, N. H. Overgaard, G. Jungersen, K. D. Garcia, A. V. Maker, L. A. Rund, H. Ozer, R. C. Gaba, and L. B. Schook, "The Oncopig Cancer Model: An Innovative Large Animal Translational Oncology Platform," *Front. Oncol.* **7**, 190 (2017).
17. S. A. Pahl, M. J. C. van Gemert, and A. J. Welch, "Determining the optical properties of turbid media by using the adding-doubling method," *Appl. Opt.* **32**(4), 559 (1993).
18. J. W. Pickering, S. A. Pahl, N. van Wieringen, J. F. Beek, H. J. Sterenborg, and M. J. van Gemert, "Double-integrating-sphere system for measuring the optical properties of tissue," *Appl. Opt.* **32**(4), 399–410 (1993).
19. W. F. Cheong, S. A. Pahl, and A. J. Welch, "A review of the optical properties of biological tissues," *IEEE J. Quantum Electron.* **26**(12), 2166–2185 (1990).
20. D. M. de Bruin, R. H. Bremmer, V. M. Kodach, R. de Kinkelder, J. van Marle, T. G. van Leeuwen, and D. J. Faber, "Optical phantoms of varying geometry based on thin building blocks with controlled optical properties," *J. Biomed. Opt.* **15**(2), 025001 (2010).
21. R. B. Saager, C. Kondru, K. Au, K. Sry, F. Ayers, and A. J. Durkin, "Multilayer silicone phantoms for the evaluation of quantitative optical techniques in skin imaging," *Proc. SPIE. Int. Soc. Opt. Eng.* **7567**(1), 756706 (2010).
22. G. Lamouche, B. F. Kennedy, K. M. Kennedy, C.-E. Bisailon, A. Curatolo, G. Campbell, V. Pazos, and D. D. Sampson, "Review of tissue simulating phantoms with controllable optical, mechanical and structural properties for use in optical coherence tomography," *Biomed. Opt. Express* **3**(6), 1381–1398 (2012).
23. M. R. N. Avanaki, A. G. Podoleanu, M. C. Price, S. A. Corr, and S. A. Hojjatoleslami, "Two applications of solid phantoms in performance assessment of optical coherence tomography systems," *Appl. Opt.* **52**(29), 7054–7061 (2013).
24. C. Yang, V. Hou, L. Y. Nelson, and E. J. Seibel, "Color-matched and fluorescence-labeled esophagus phantom and its applications," *J. Biomed. Opt.* **18**(2), 026020 (2013).
25. K. L. Lurie, G. T. Smith, S. A. Khan, J. C. Liao, and A. K. Ellerbee, "Three-dimensional, distensible bladder phantom for optical coherence tomography and white light cystoscopy," *J. Biomed. Opt.* **19**(3), 1 (2014).
26. P. Diep, S. Pannem, J. Sweer, J. Lo, M. Snyder, G. Stueber, Y. Zhao, S. Tabassum, R. Istfan, J. Wu, S. Erramilli, and D. Roblyer, "Three-dimensional printed optical phantoms with customized absorption and scattering properties," *Biomed. Opt. Express* **6**(11), 4212–4220 (2015).
27. S. E. Bohndiek, S. Bodapati, D. Van De Sompel, S.-R. Kothapalli, and S. S. Gambhir, "Development and application of stable phantoms for the evaluation of photoacoustic imaging instruments," *PLoS One* **8**(9), e75533 (2013).
28. T. Moffitt, Y.-C. Chen, and S. A. Pahl, "Preparation and characterization of polyurethane optical phantoms," *J. Biomed. Opt.* **11**(4), 041103 (2006).
29. C.-E. Bisailon, G. Lamouche, R. Maciejko, M. Dufour, and J.-P. Monchalain, "Deformable and durable phantoms with controlled density of scatterers," *Phys. Med. Biol.* **53**(13), N237–247 (2008).
30. B. F. Kennedy, S. Loitsch, R. A. McLaughlin, L. Scolaro, P. Rigby, and D. D. Sampson, "Fibrin phantom for use in optical coherence tomography," *J. Biomed. Opt.* **15**(3), 030507 (2010).
31. M. S. Wróbel, A. P. Popov, A. V. Bykov, V. V. Tuchin, and M. Jędrzejewska-Szczerska, "Nanoparticle-free tissue-mimicking phantoms with intrinsic scattering," *Biomed. Opt. Express* **7**(6), 2088–2094 (2016).
32. D. Fixler, T. Nayhoz, and K. Ray, "Diffusion Reflection and Fluorescence Lifetime Imaging Microscopy Study of Fluorophore-Conjugated Gold Nanoparticles or Nanorods in Solid Phantoms," *ACS Photonics* **1**(9), 900–905 (2014).
33. R. Ankri, H. Taitelbaum, and D. Fixler, "Reflected light intensity profile of two-layer tissues: phantom experiments," *J. Biomed. Opt.* **16**(8), 085001 (2011).
34. I. Çilesiz, P. Fockens, R. Kerindongo, D. Faber, G. Tytgat, F. ten Kate, and T. van Leeuwen, "Comparative optical coherence tomography imaging of human esophagus: How accurate is localization of the muscularis mucosae?" *Gastrointest. Endosc.* **56**(6), 852–857 (2002).
35. R. Wessels, D. D. de Bruin, D. Faber, T. G. van Leeuwen, M. van Beurden, and T. Ruers, "Optical biopsy of epithelial cancers by optical coherence tomography (OCT)," *Lasers Med. Sci.* 1291 (2013).
36. J. Baxi, W. J. Calhoun, Y. J. Sepah, D. X. Hammer, I. K. Ilev, T. J. Pfefer, Q. D. Nguyen, and A. Agrawal, "Retina-simulating phantom for optical coherence tomography," *J. Biomed. Opt.* **6**(1), 10 (2013).
37. N. Zulina, O. Caravaca, S. Gravelyn, L. Zorn, and M. Gora, "Colorectal polyps mimicking phantoms for OCT application," in *Clinical and Preclinical Optical Diagnostics II* (2019), Paper 11073\_52 (Optical Society of America, 2019), p. 11073\_52.



38. C.-É. Bisaillon and G. Lamouche, "Artery phantoms for intravascular optical coherence tomography: diseased arteries," *J. Biomed. Opt.* **18**(9), 096010 (2013).
39. G. T. Smith, K. L. Lurie, S. A. Khan, J. C. Liao, and A. K. Ellerbee, "Multilayered disease-mimicking bladder phantom with realistic surface topology for optical coherence tomography," in *Design and Performance Validation of Phantoms Used in Conjunction with Optical Measurement of Tissue VI* (International Society for Optics and Photonics, 2014), 8945, p. 89450E.
40. A. Agrawal, T. J. Pfefer, N. Gilani, and R. Drezek, "Three-dimensional characterization of optical coherence tomography point spread functions with a nanoparticle-embedded phantom," *Opt. Lett.* **35**(13), 2269–2271 (2010).
41. J. H. Chandler, F. Mushtaq, B. Moxley-Wyles, N. P. West, G. W. Taylor, and P. R. Culmer, "Real-Time Assessment of Mechanical Tissue Trauma in Surgery," *IEEE Trans. Biomed. Eng.* **64**(10), 2384–2393 (2017).
42. Participants in the Paris Workshop, "The Paris endoscopic classification of superficial neoplastic lesions: esophagus, stomach, and colon: November 30 to December 1, 2002," *Gastrointest. Endosc.* **58**(6 Suppl), S3–S43 (2003).
43. L. Bujanda, A. Cosme, I. Gil, and J. I. Arenas-Mirave, "Malignant colorectal polyps," *World J. Gastroenterol.* **16**(25), 3103–3111 (2010).
44. M. Yamada, Y. Saito, H. Imaoka, M. Saiko, S. Yamada, H. Kondo, H. Takamaru, T. Sakamoto, J. Sese, A. Kuchiba, T. Shibata, and R. Hamamoto, "Development of a real-time endoscopic image diagnosis support system using deep learning technology in colonoscopy," *Sci. Rep.* **9**(1), 14465 (2019).
45. X. Wen, Z. Mao, Z. Han, V. V. Tuchin, and D. Zhu, "In vivo skin optical clearing by glycerol solutions: mechanism," *J. Biophotonics* **3**(1–2), 44–52 (2009).
46. A. Ron, N. Racheli, I. Breskin, and R. Shechter, "A tissue mimicking phantom model for applications combining light and ultrasound," *Proc. SPIE. Int. Soc. Opt. Eng.* **8583**(1), 858307 (2013).
47. V. Westphal, A. M. Rollins, S. Radhakrishnan, and J. A. Izatt, "Correction of geometric and refractive image distortions in optical coherence tomography applying Fermat's principle," *Opt. Express* **10**(9), 397–404 (2002).
48. R. C. Gonzalez, *Digital Image Processing* (Pearson Education, 2009).
49. J. Zhang, W. Yuan, W. Liang, S. Yu, Y. Liang, Z. Xu, Y. Wei, and X. Li, "Automatic and robust segmentation of endoscopic OCT images and optical staining," *Biomed. Opt. Express* **8**(5), 2697–2708 (2017).
50. A. J. Trindade, A. Rishi, R. Hirtten, S. Inamdar, D. V. Sejal, and J.-F. Colombel, "Identification of volumetric laser endomicroscopy features of colon polyps with histologic correlation," *Gastrointest. Endosc.* **87**(6), 1558–1564 (2018).
51. A. Lozzi, A. Agrawal, A. Boretsky, C. G. Welle, and D. X. Hammer, "Image quality metrics for optical coherence angiography," *Biomed. Opt. Express* **6**(7), 2435 (2015).
52. G. Simone, M. Pedersen, and J. Y. Hardeberg, "Measuring perceptual contrast in digital images," *J. Vis. Commun. Image Represent.* **23**(3), 491–506 (2012).
53. H. Nguyen, C. Loustaunau, A. Facista, L. Ramsey, N. Hassounah, H. Taylor, R. Krouse, C. M. Payne, V. L. Tsikitis, S. Goldschmid, B. Banerjee, R. F. Perini, and C. Bernstein, "Deficient Pms2, ERCC1, Ku86, CcOI in Field Defects During Progression to Colon Cancer," *J. Visualized Exp.* (41), (2010).
54. K. Liang, O. O. Ahsen, Z. Wang, H.-C. Lee, W. Liang, B. M. Potsaid, T.-H. Tsai, M. G. Giacomelli, V. Jayaraman, H. Mashimo, X. Li, and J. G. Fujimoto, "Endoscopic forward-viewing optical coherence tomography and angiography with MHz swept source," *Opt. Lett.* **42**(16), 3193–3196 (2017).
55. A. N. Bashkatov, E. A. Genina, V. I. Kochubey, V. S. Rubtsov, E. A. Kolesnikova, and V. V. Tuchin, "Optical properties of human colon tissues in the 350–2500 nm spectral range," *Quantum Electron.* **44**(8), 779–784 (2014).